

STRUCTURAL AND ELECTROCHEMICAL CHARACTERISTICS OF GRAPHENE NANOSHEETS AS SUPERCAPACITOR ELECTRODES

Gomaa A.M. Ali^{1,2}, Salah A. Makhlouf^{3,4}, Mashitah M. Yusoff¹
and Kwok Feng Chong¹

¹Faculty of Industrial Sciences and Technology, Universiti Malaysia Pahang, Gambang, 26300 Kuantan, Malaysia

²Chemistry Department, Faculty of Science, Al-Azhar University, Assiut, 71524, Egypt

³Physics Department, Faculty of Science, Assiut University, Assiut 71516, Egypt

⁴Deanship of Scientific Research, Al Imam Mohammad Ibn Saud Islamic University (IMSIU), Riyadh, 11463, Saudi Arabia

Received: February 15, 2015

Abstract. In this paper, graphene oxide (GO) was prepared by the Hummers' method and reduced using hydrazine to produce graphene nanosheets (GNS). Physicochemical characterizations of the prepared materials were performed using XRD, FTIR, TGA, DTA, BET, UV-vis, Raman, and FESEM techniques. The results elucidate the structure, morphology, mesoporosity and thermal stability of the prepared samples. Detailed electrochemical studies have been conducted on GNS by CV, galvanostatic and complex impedance measurements indicating some interesting features. GNS shows a specific capacitance of 140 F g⁻¹ at 0.05 A g⁻¹. GNS shows high cyclic stability of about 86% over 1100 cycles at a current density of 1 A g⁻¹. The large electrochemical active surface area suggests that most of the nanosheets are accessible to ions adsorption in the electrolyte system. Impedance spectra show low resistance of GNS, supporting its suitability for supercapacitor electrode applications.

1. INTRODUCTION

Supercapacitors, also known as ultracapacitors, are electrochemical energy storage devices with higher capacity than physical capacitors, furthermore their charging-discharging rate capability is higher than that of batteries. Two types of supercapacitors are known, namely electrochemical double layer capacitors (EDLCs) and pseudocapacitors. The former one stores energy non-faradically through the accumulation of charges at the electrode–electrolyte interface, whereas the latter stores energy faradically by the redox reaction [1-4]. EDLCs usually contain carbon based materials possessing high surface area as the electrode material, and the capacitance

originates from the charge accumulation at the interface between electrode and electrolyte [5,6]. On the other hand, pseudocapacitors employ transition metal oxides [2,3,7-9] or conductive polymers [10,11] as the electrode material. Though the energy densities in pseudocapacitors are higher than that of EDLCs, the faradic reactions within pseudocapacitors could lead to phase changes and limit their life time [12].

Graphene is atomically thin two dimensional (2D) system of sp² carbon atoms organized in hexagonal lattice structure. Graphene has been found to be of both fundamental interest and suitable for a wide range of potential applications. The porous

Corresponding author: Gomaa A.M. Ali, e-mail: gomaasanad@gmail.com and gomaasanad@azhar.edu.eg

nature of the electrode material facilitates ion transport processes, and therefore improves the performance of supercapacitors. Graphene nanosheets (GNS) represents an outstanding candidate for supercapacitor electrodes due their large in-plane conductivity, high specific surface area, strength as well as both of its major surfaces are exterior surfaces ready susceptible for electrolyte ions [13]. Graphene oxide (GO) has been synthesized by Brodie, Staudenmaier, Hummers, and modified Hummers methods [14], and graphene has been obtained from GO by chemical [15], electrochemical [16], thermal [17], and solvothermal [18] reductions. The degree of GO reduction depends on the reduction route and has a significant effect on the physical properties of the obtained material.

In this work, GO had been prepared from graphite by the Hummers' method and subsequently reduced by hydrazine to produce GNS. The physicochemical properties of both GO and GNS had been studied by X-ray diffraction (XRD), Fourier transform infrared spectroscopy (FTIR), thermal analysis (TGA/DTA), nitrogen (N_2) adsorption-desorption technique, ultra-violet (UV-vis), Raman spectroscopy and field emission scanning electron microscopy (FESEM). Detailed electrochemical studies were conducted by cyclic voltammetry (CV), charge-discharge galvanostatic tests and electrochemical impedance spectroscopy (EIS).

2. EXPERIMENTAL PROCEDURES AND TECHNIQUES

2.1. Sample preparation

In order to prevent incomplete oxidation, graphite powder (Merck) was pre-oxidized by slowly mixing 20 g of graphite, 10 g of $K_2S_2O_8$, and 10 g of P_2O_5 into 30 mL of concentrated H_2SO_4 , while stirring. The reaction mixture was heated up to 80 °C using an oil bath with continuous stirring for 6 h. The mixture was then diluted with distilled water, filtered and washed until the filtrate became neutral in pH. The washed powder was dried overnight in a vacuum oven at 60 °C. The pre-oxidized graphite powder was oxidized by the Hummers' method as follows: 20 g of the pre-oxidized graphite powder was added to 460 mL of concentrated H_2SO_4 in an ice bath. 60 g of $KMnO_4$ was then slowly added while stirring. The mixture was heated up to 35 °C for 2 h before 1 L of distilled water was added. The stirring was continued for 15 min and additional 3 L of distilled water and 50 mL of 30% H_2O_2 were added into the mixture. The mixture was filtered, washed with 1:10 aqueous HCl and dried overnight at 60 °C in vacuum

to obtain dry graphite oxide. Exfoliation of graphite oxide was done by sonicating graphite oxide dispersion (2 gL^{-1}) at 200 W for 30 min. The dispersion was later centrifuged at 6000 rpm for 10 min, to remove the unexfoliated graphite oxide. The homogeneous yellow brown supernatant was obtained as GO dispersion. GNS was prepared by adding 0.34 mL of hydrazine monohydrate into 50 mL of GO dispersion and the pH was adjusted to 10. The mixture was refluxed at 95 °C for 24 h, dried by vacuum filtration, washed with distilled water and finally dried overnight in vacuum.

2.2. Sample characterizations

The crystal structure was analyzed using a Rigaku X-ray diffractometer (Miniflex II with $Cu-K_{\alpha}$ radiation at 40 kV, 30 mA, $\lambda = 1.5406\text{ \AA}$) within the 2θ range of 5° to 80° at a scanning rate of $0.02\text{ \theta s}^{-1}$ with a step time of 2 s. The functional groups were examined using a Perkin Elmer (Spectrum 100) infrared spectrophotometer over the range of 400-4000 cm^{-1} . The thermal stability was tested with a TA Instruments (Q500) thermal analyzer up to 900 °C at a heating rate of $10\text{ }^{\circ}C\text{ min}^{-1}$ in air and N_2 environments. The GO reduction was confirmed using a Thermo Scientific (Genesys 10S) UV spectrophotometer at room temperature. Raman spectra were obtained using Raman Microscope (Invia, Renishaw, UK) with 532 nm laser excitation. The surface morphology was monitored by a JEOL (JSM-7800F) field emission scanning electron microscope (FESEM). Specific surface area and pore size distribution of the samples were measured by N_2 adsorption-desorption technique (NOVA-3200, USA). The samples were degassed at 250 °C for 3 h before analysis and the N_2 isotherms were obtained at -196 °C. The specific surface area was calculated using the Brunauer-Emmett-Teller (BET) method. The pore size distributions were determined by applying the Barrett-Joyner-Halenda (BJH) model to the N_2 desorption branches.

2.3. Electrochemical studies

The electrode was made by mixing GNS with 5 wt.% polytetrafluoroethylene (PTFE) and 15 wt.% carbon black. The electrochemical tests were performed using a two-electrode system, in which two electrodes are electrically isolated from each other by porous membrane pre-soaked with 5 M KOH electrolyte. The data were collected using an electrochemical workstation (Autolab/PGSTAT M101) equipped with a frequency response analyser. Cyclic voltammetry tests were performed between 0

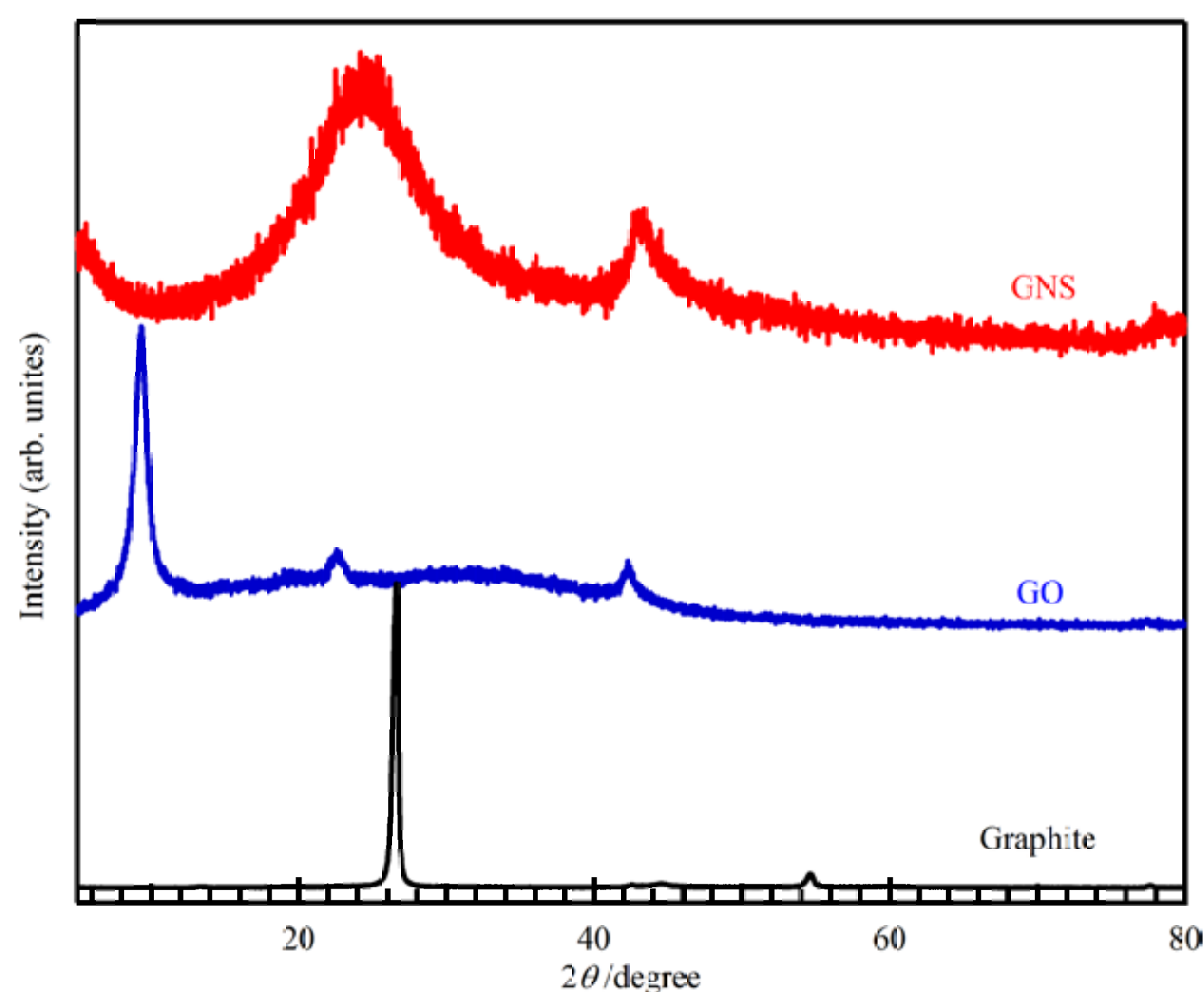


Fig. 1. XRD patterns of graphite, GO, and GNS.

and 1 V with scan rates range from 5 to 100 mV s⁻¹. Charge-discharge galvanostatic tests were performed at current densities up to 1 A g⁻¹. Impedance data were collected from 50 kHz to 0.01 Hz with ac amplitude at 10 mV.

3. RESULTS AND DISCUSSION

3.1. X-Ray diffraction

Fig. 1 compares the XRD patterns of graphite, GO and GNS. For graphite, the major (002) peak appears at 26.5° with a d-spacing of 3.35 Å, and other minor peaks at 44.6°, 54.7°, and 77.5° are observed and indexed according to ICDD 00-023-0064 card [19,20]. The main (002) peak of GO is located at 9.8° with a d-spacing of 9.43 Å. The large expansion of d-spacing of GO compared to graphite is usually ascribed to the insertion of oxygen-containing groups and H₂O molecules [19]. Two other peaks at 23° and 43° are detected and could be ascribed to the limited ordering of few-layers in GO and

turbostratic band of disordered carbon materials, respectively [21]. GNS shows diffraction peaks at 24.86° and 43.10° related to the (002) and (100) crystallographic planes of its structure, respectively [22]. Disappearance of the 9.8° peak in GNS indicates that graphite oxide is typically reduced to graphene.

3.2. FTIR spectra

Fig. 2 shows the FTIR spectra of graphite, GO and GNS. Presence of the vibrational bands due to carboxyl (1410 cm⁻¹), epoxy (1220 cm⁻¹), as well as bands attributable to alkoxy (1060 cm⁻¹) confirms the oxide functional groups situated at the edges of the GO [1,14,19,23]. The absorption band at 1740 cm⁻¹ is due to the C=O stretching in COOH groups [17]. The disappearance of this band in GNS confirms the reduction of the carbonyl groups in GO structure. The band at 1610 cm⁻¹ which appears for all samples is attributed to C–C stretching vibration [23]. The characteristic absorption bands of oxygen–contained groups, such as the intense band of O–H groups of adsorbed water appears for all samples at 3440 cm⁻¹.

3.4. Thermal analysis

Thermal gravimetric analysis (TGA) and differential thermo gravimetric analysis (DTA) curves for GO and GNS in air and N₂ atmospheres are shown in Fig. 3. For GO in atmospheric air, 18% water loss occurs at temperatures less than 100 °C. The second weight loss stage of 42% occurs at around 200 °C, and corresponds to the decomposition of labile oxygen groups such as carboxylic groups [24]. GO is fully decomposed in air above 750 °C. On the other hand, GO exhibits lower weight loss value in N₂ atmosphere. The three weight loss stages correspond

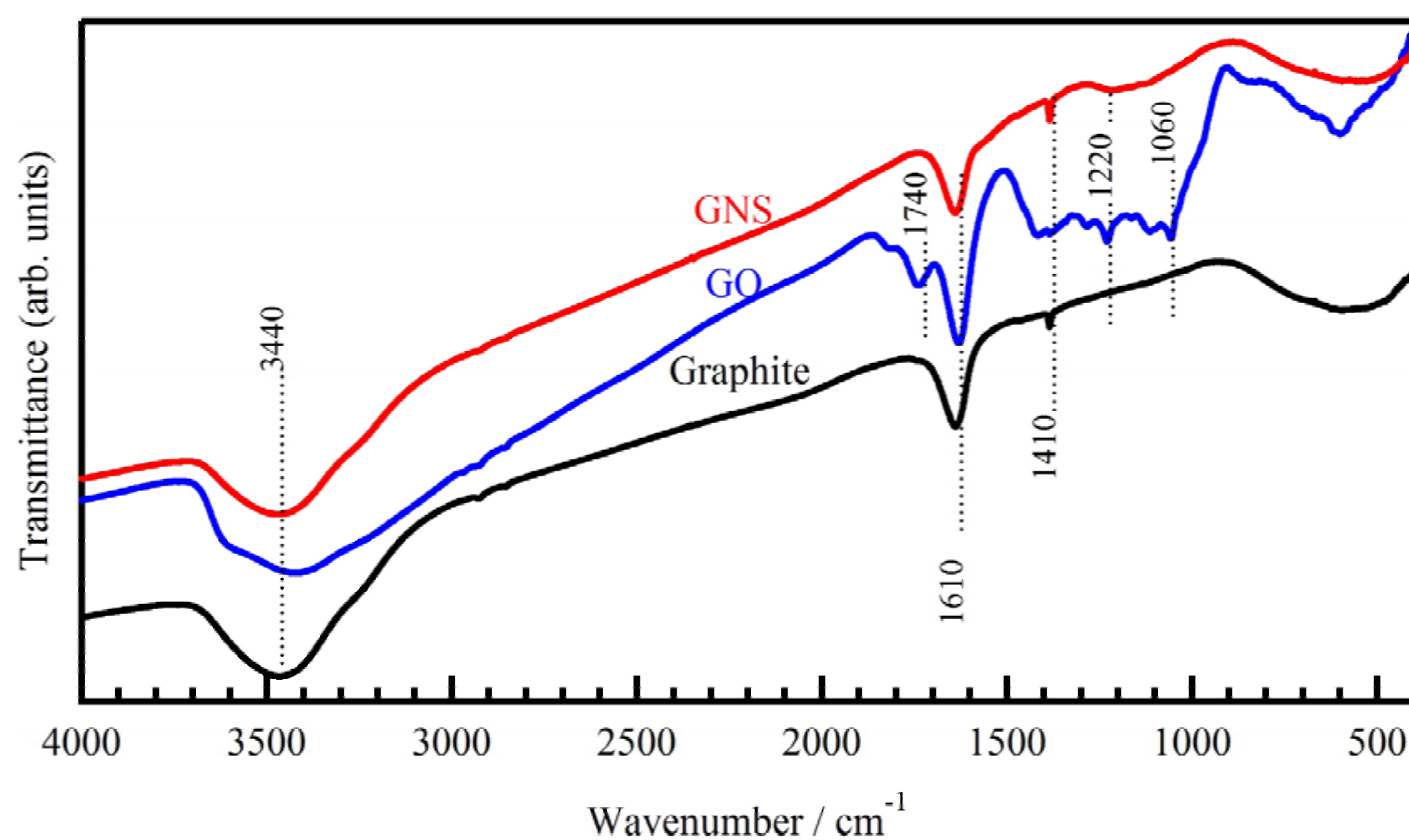


Fig. 2. FTIR spectra of graphite, GO, and GNS.

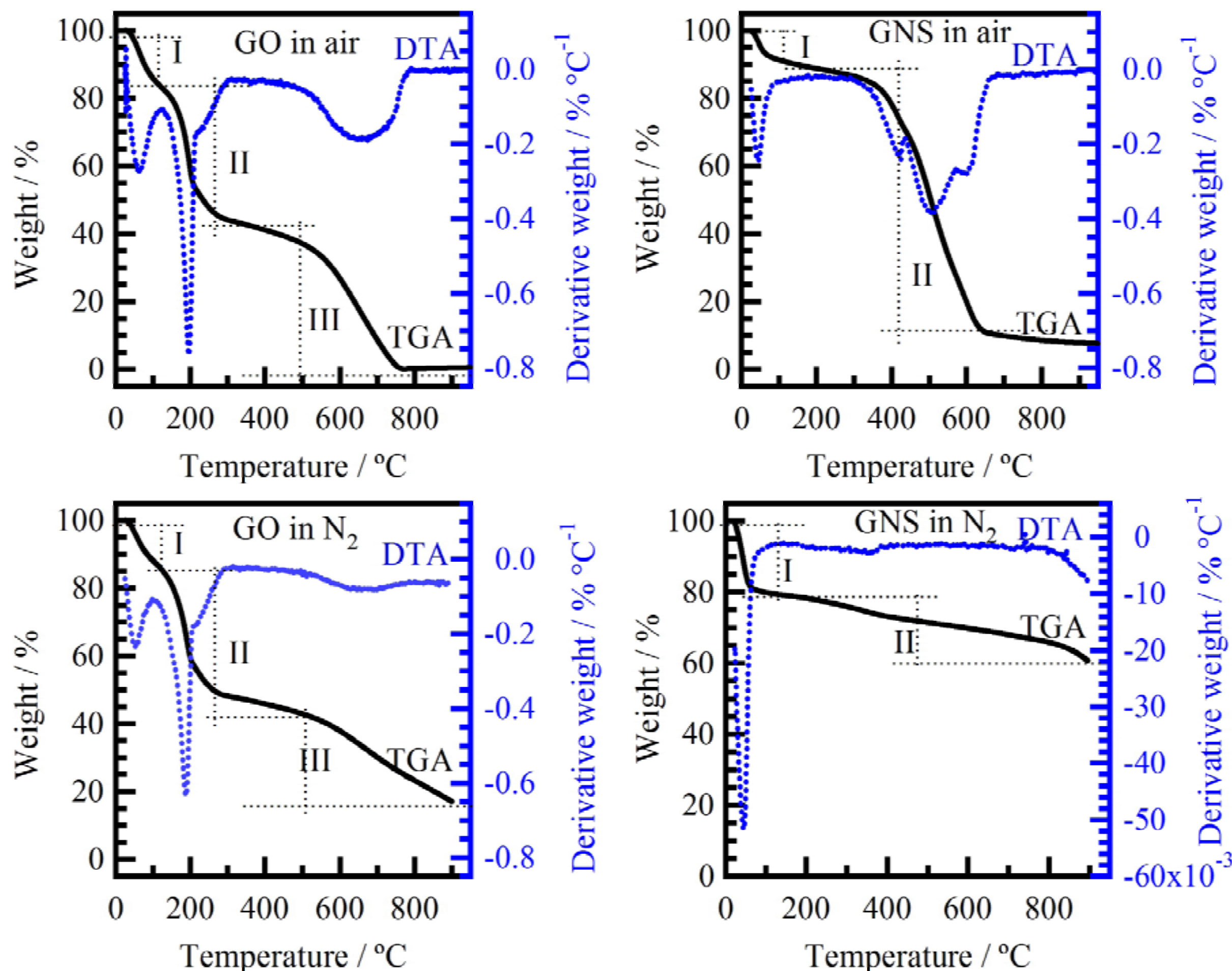


Fig. 3. TGA and DTA curves for GO, and GNS.

to the three DTA peaks observed at 70 °C, 200 °C, and 650 °C, respectively. The results are consistent with the fact that GO is thermally stable in air only up to 600 °C, by virtue of the reduced van der Waals forces [24,25]. GNS shows two weight loss stages in atmospheric air, stage I, 10% at around 50 °C and stage II, 80% at around 600 °C. These stages are related to the removal of adsorbed surface water and GNS structural decomposition, respectively. Simultaneously, two DTA peaks are observed at around 70 and 550 °C. No weight loss occurs at 300 °C, indicating that the oxygen-containing groups in GNS had been completely reduced. The results also show that GNS structure has less amount of adsorbed water than GO. In N₂ atmosphere, GNS shows two weight loss stages that sum up to about 40%, close to that reported by other authors [26], indicating that GNS structure does not decompose under N₂ environment.

3.3. N₂ adsorption–desorption technique

Fig. 4 shows the N₂ adsorption-desorption isotherms of GO and GNS, and the insets show the pore size distribution. The isotherms exhibit type IV curves characterized by hysteresis loops confirming the mesoporous structures of both GO and GNS [13]. Pore size distribution curves show that the pore size ranges from 2 to 4 nm for GO and from 2 to 6 nm for GNS. It also shows that GNS has larger pore size and volume, which can be attributed to appearance

of more pores via removal of functional groups in the GO. These mesopores play an important role in enhancing the adsorption of ions during the electrochemical measurements. The specific surface area obtained are 47.7 and 124.1 m² g⁻¹ for GO and GNS, respectively. The smaller value obtained for GNS as compared to the theoretical value of 2600 m² g⁻¹ for graphene could be due to the incomplete exfoliation of GO and agglomerations of graphene layers during the reduction process [27].

3.4. UV–vis absorption and Raman spectra

Further insights to the electronic conjugation of GO and GNS can be obtained from UV–vis absorption spectra as shown in Fig. 5a. The main absorption peaks located at 230 and 268 nm refer to GO and GNS, respectively [28,29]. The spectrum of GO dispersion presents two characteristic features: a maximum at 230 nm corresponding to π/π^* transitions of aromatic C–C bonds and a hump at around 303 nm assigned to n/π^* transitions of C=O bonds. The 268 nm peak indicates the restoration of π conjugation within graphene sheets [16,26].

Fig. 5b shows the Raman spectra of GO and GNS exhibiting D and G bands at 1347 cm⁻¹ and 1586 cm⁻¹, respectively. The appearance of D band is a sign of disorder in the carbon lattice. The intensity ratio of D and G bands (I_D/I_G) is a measure of disorder, representing the sp²/sp³ carbon ratio. The I_D/I_G ratio for GNS was 0.99 which is larger than

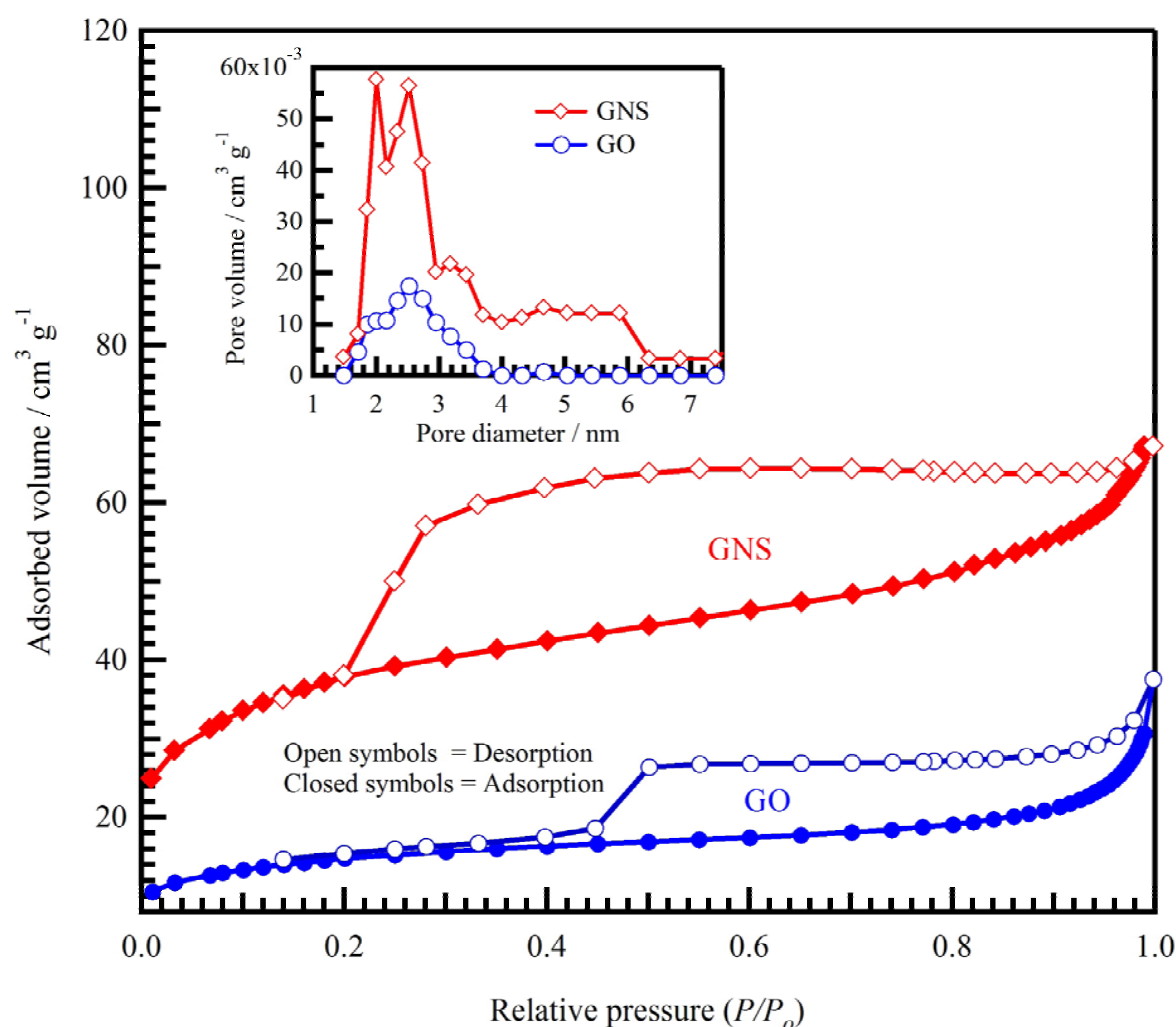


Fig. 4. N_2 adsorption–desorption isotherm of GO and GNS, the insets are the pore size and volume distributions.

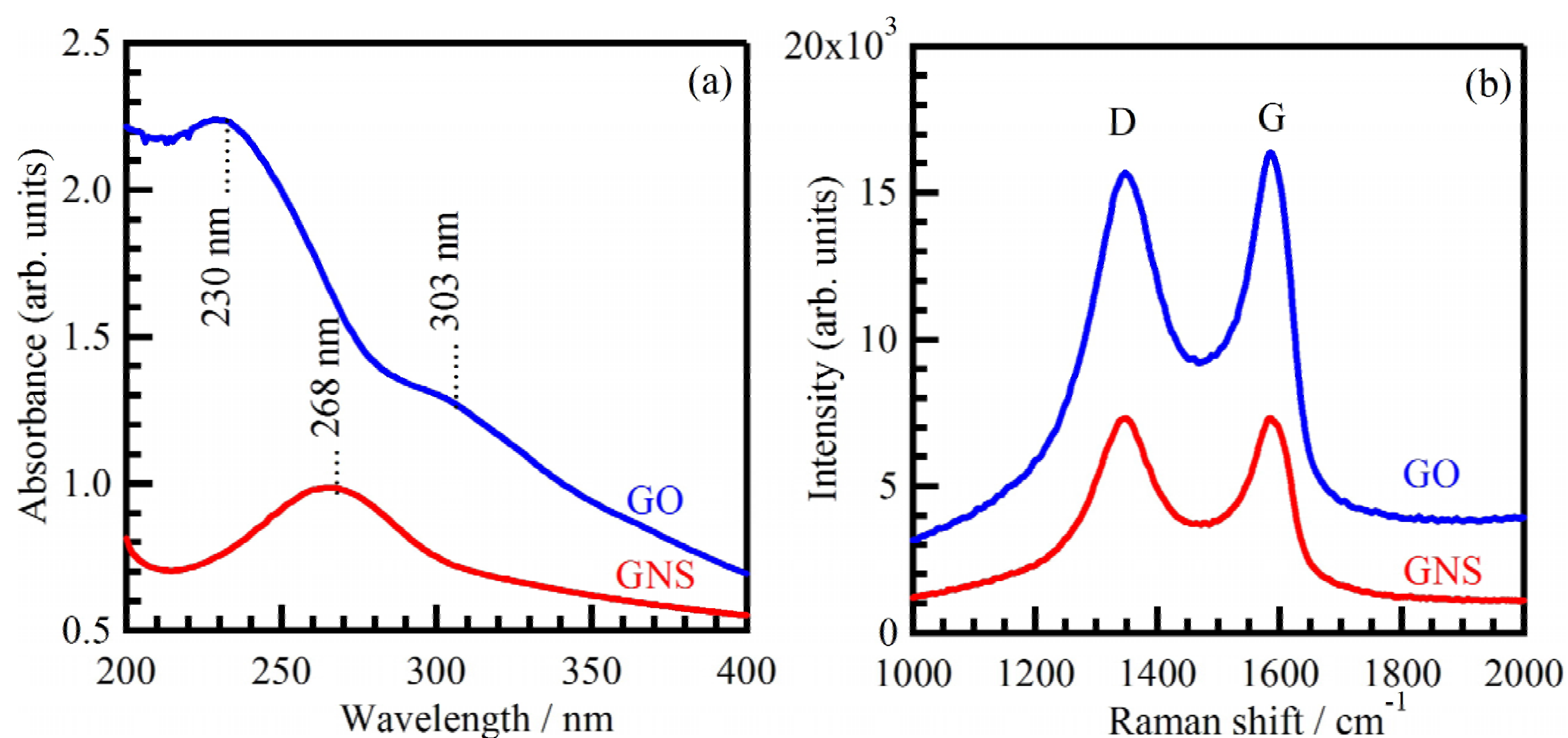


Fig. 5. UV–vis absorption (a) and Raman (b) spectra of GO and GNS.

0.95 found for GO due to the reduction effect [21]. These findings indicate that the in-plane sp^2 domains of GNS are smaller in size than those of GO, but more numerous in number as a result of oxygen removal by reduction [26].

3.5. FESEM

Figs. 6a and 6b show FESEM images for GO and GNS, respectively. The inset shows an image of higher magnification for GNS. GO shows agglomeration of the non-exfoliated platelets, whereas that of GNS shows exfoliated nanosheets resulted from

the removal of carbonyl, hydroxyl and carboxylic groups by reduction. The nanosheets structure of GNS supports the BET findings of high surface area and large pore size.

3.6. Cyclic voltammetry and galvanostatic charge-discharge

Fig. 7 shows cyclic voltammetry curves at different scan rates for GNS. CV curves exhibit rectangular-like shapes and symmetrical around zero with no any obvious redox peaks, which reveal the ideal capacitive behaviour. Fig. 8a shows the charge-dis-

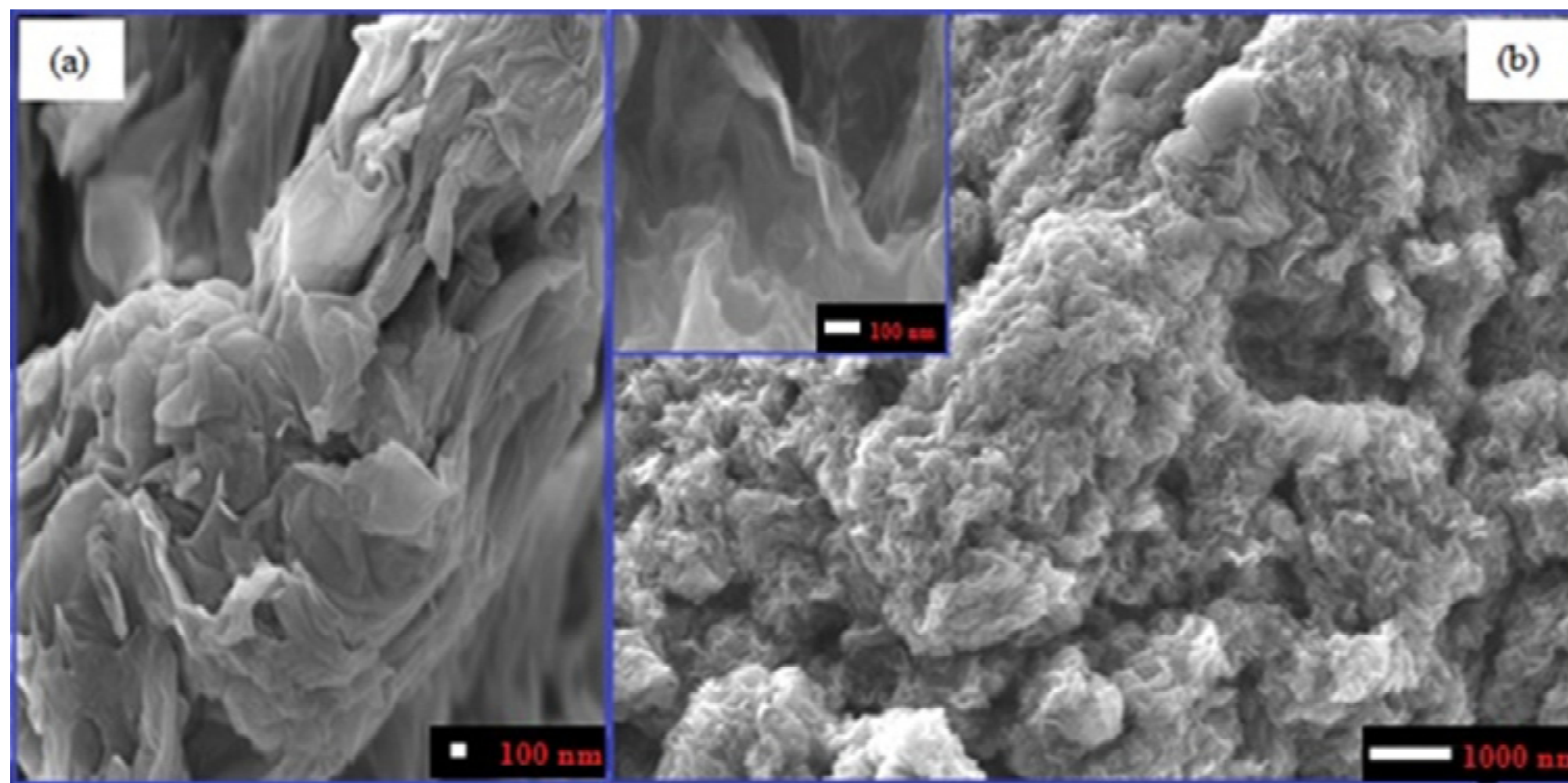


Fig. 6. FESEM images of (a) GO and (b) GNS.

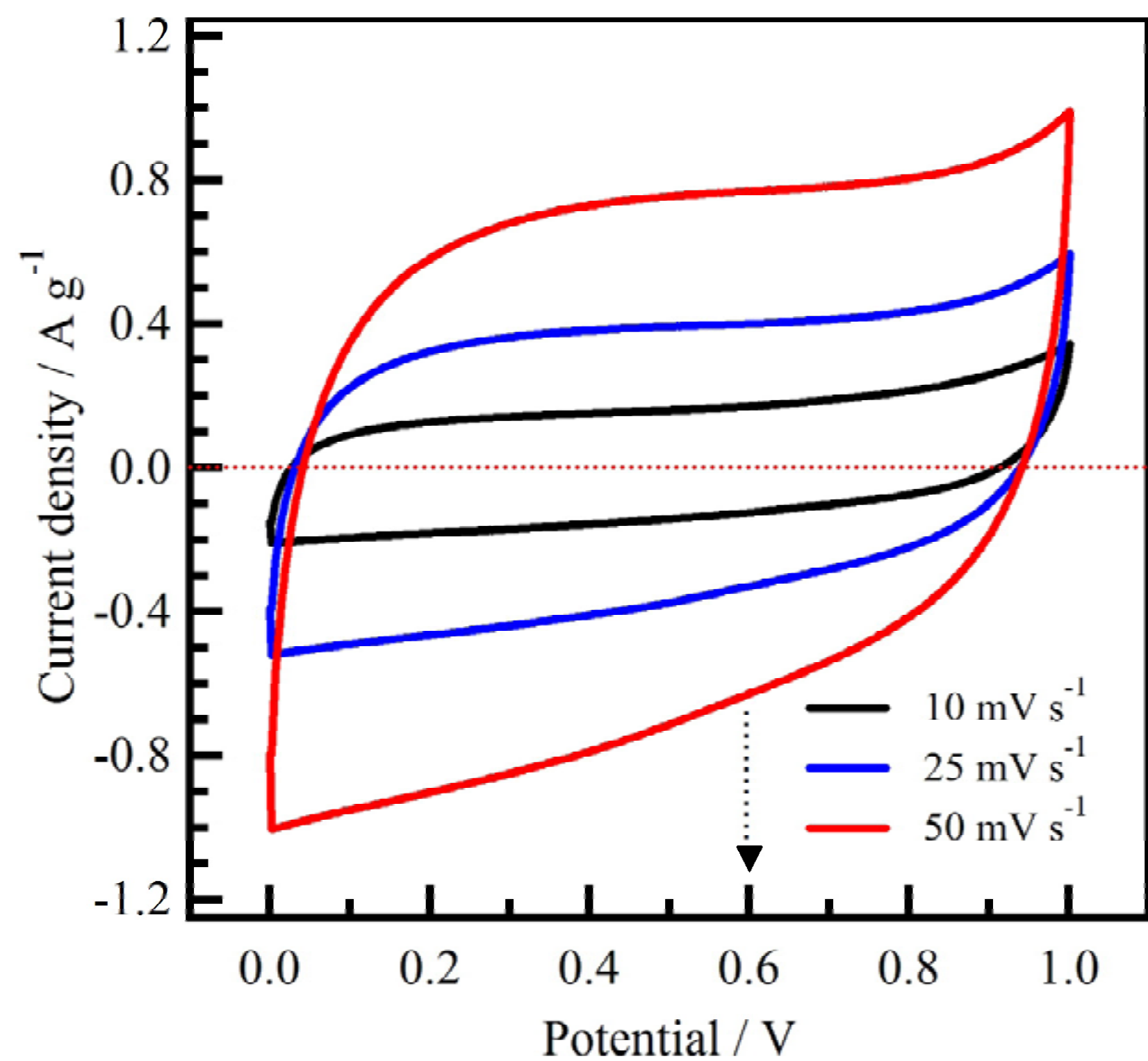


Fig. 7. Cyclic voltammetry curves at different scan rates for GNS.

charge curves for GNS in 5 M KOH solution in the range from 0 to 1 V for representative current densities between 0.05 A g^{-1} and 1 A g^{-1} . Linear charge

and discharge curves with neglected iR drop of about 2.1% at 0.25 A g^{-1} is obtained, indicating that the electrodes have low internal resistance which lead to better EDL performance. The specific capacitance for single GNS electrode can be calculated by the equation reported elsewhere [6,30-32]. The specific capacitance of GNS was found to be 140 F g^{-1} at 0.05 A g^{-1} (see Fig. 8b), which is higher than 80 F g^{-1} at 0.025 A g^{-1} [33] and the reported value for chemically modified graphene in aqueous electrolytes [12].

The long life stability is a very important factor in supercapacitor applications. As shown in Fig. 9 (left vs. bottom), GNS shows high cyclic stability reaching 86% of its original values at 1 A g^{-1} over 1100 cycles. It also shows a high columbic efficiency of about 88% over all cycling range. The inset of Fig. 9 shows that the charge-discharge curves remain linear for all stability cycles, indicating insignificant change in the specific capacitance.

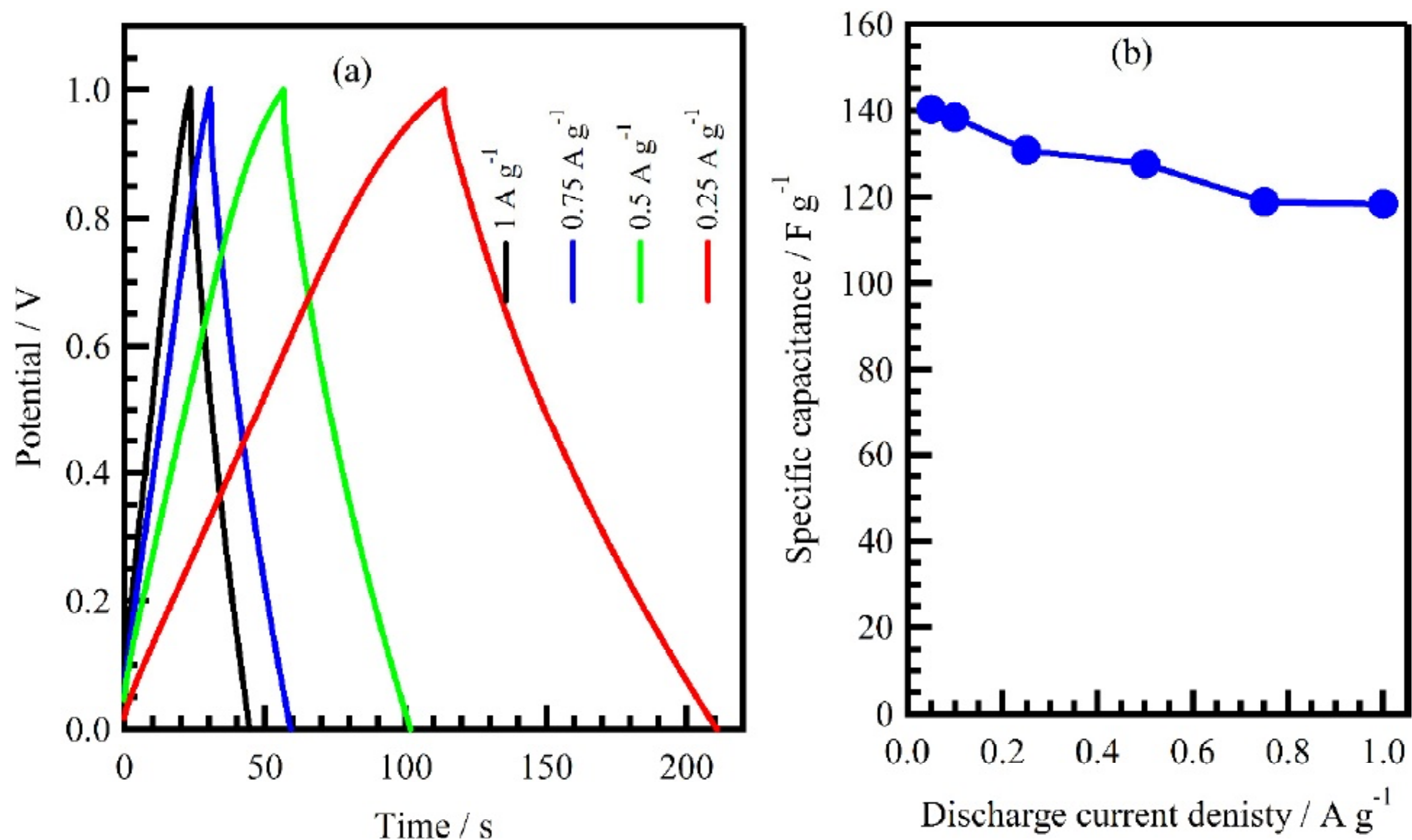


Fig. 8. Galvanostatic charge-discharge curves at different current densities (a) and specific capacitance as a function of current density (b), for GNS.

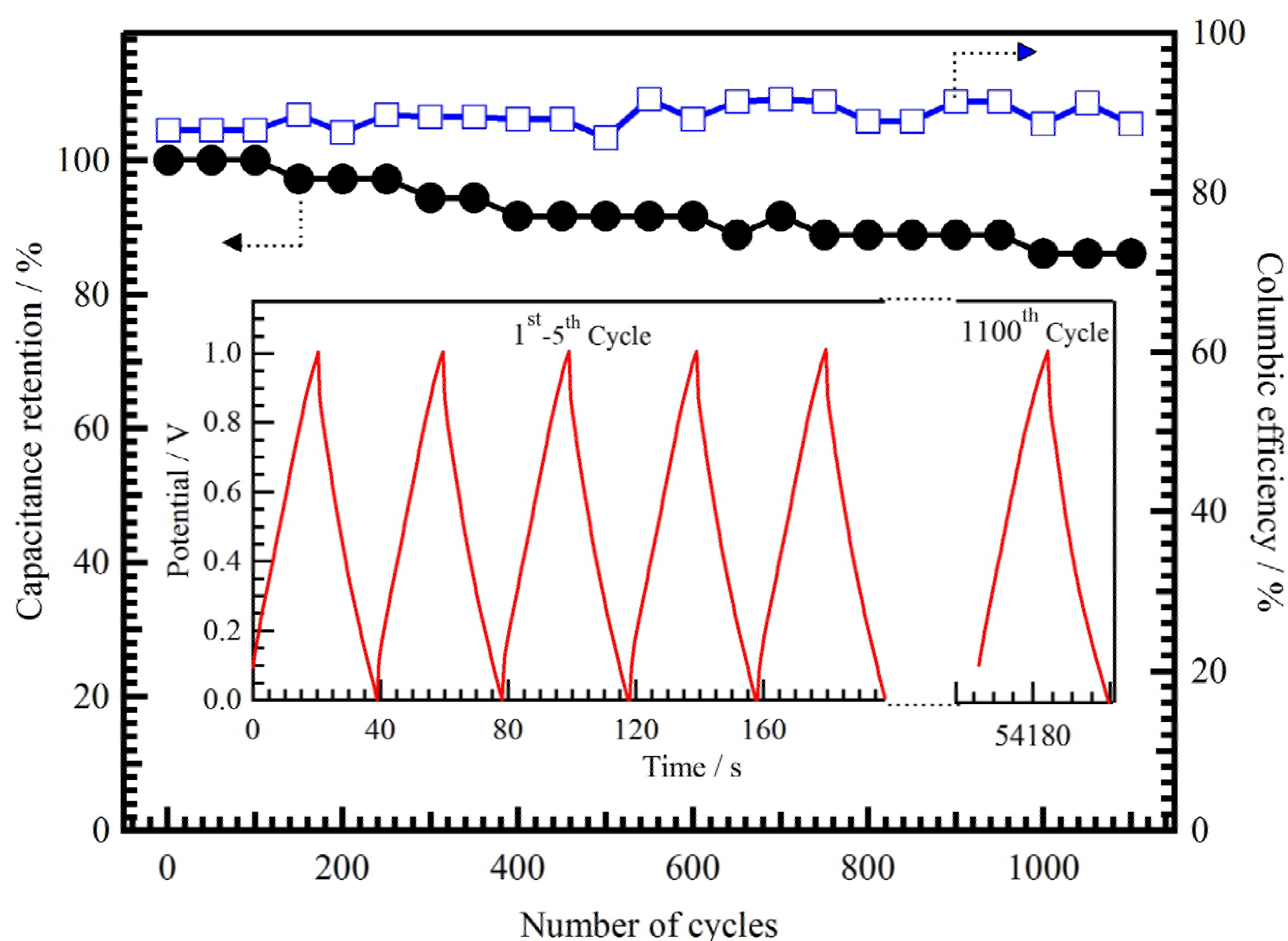


Fig. 9. Cycle life stability curves (left vs. bottom) and columbic efficiency (right vs. bottom) at 1 A g^{-1} current density for GNS, the insets show the charge-discharge curves for different cycles.

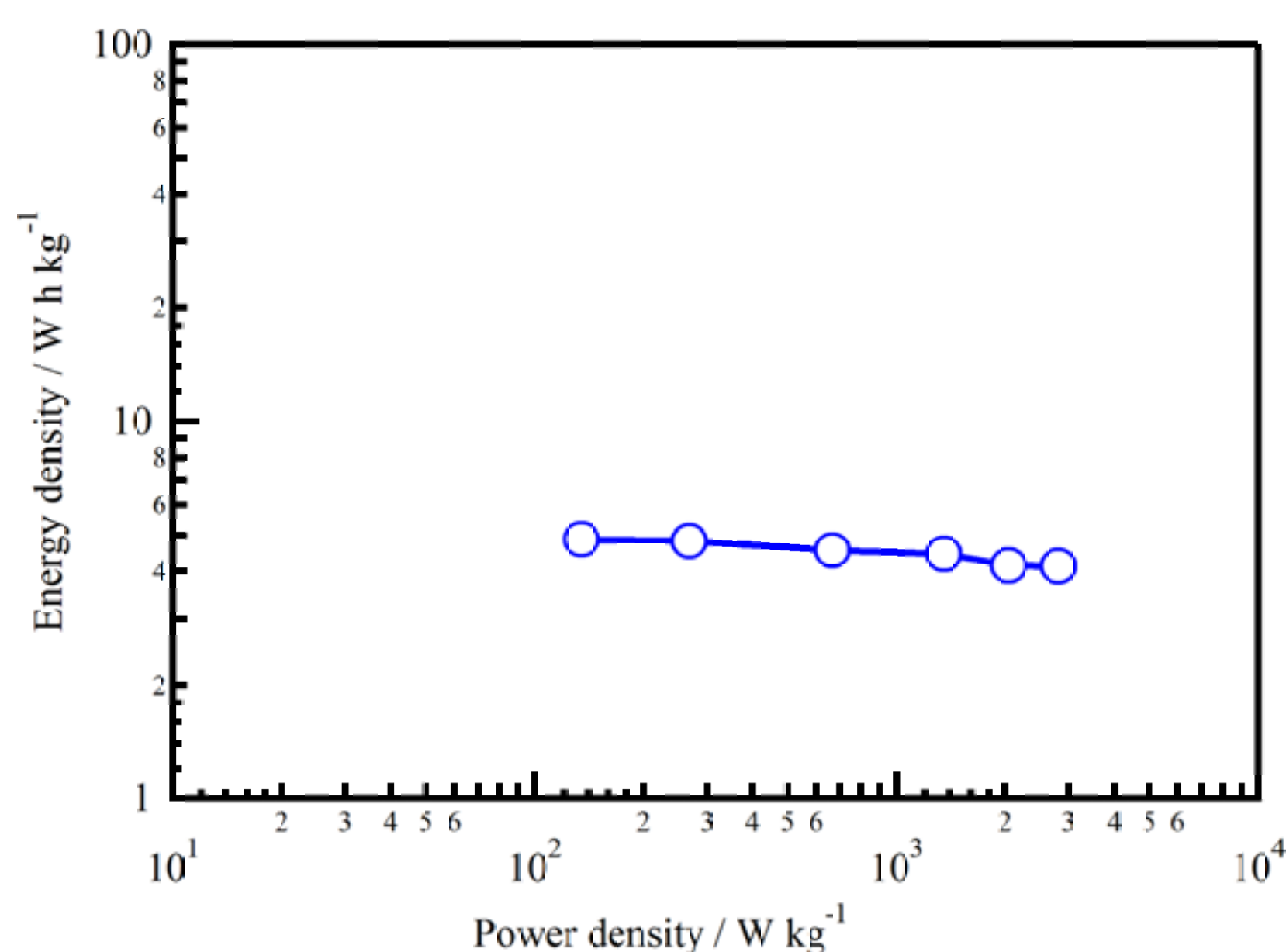


Fig. 10. Ragone plot for GNS.

The energy (E) and power (P) densities can be calculated from charge-discharge data using the equations as reported in reference [13]. The Ragone plot for GNS is shown in Fig. 10, showing that the energy density ranges from 5 to 4 W h kg^{-1} and power density ranges from 135 to 2818 W h kg^{-1} for discharge current that ranges from 0.05 and 1 A g^{-1} .

3.7. Impedance spectra

Fig. 11a shows *Nyquist* plot obtained in 5 M KOH for the frequency range 50 kHz–0.01 Hz at open

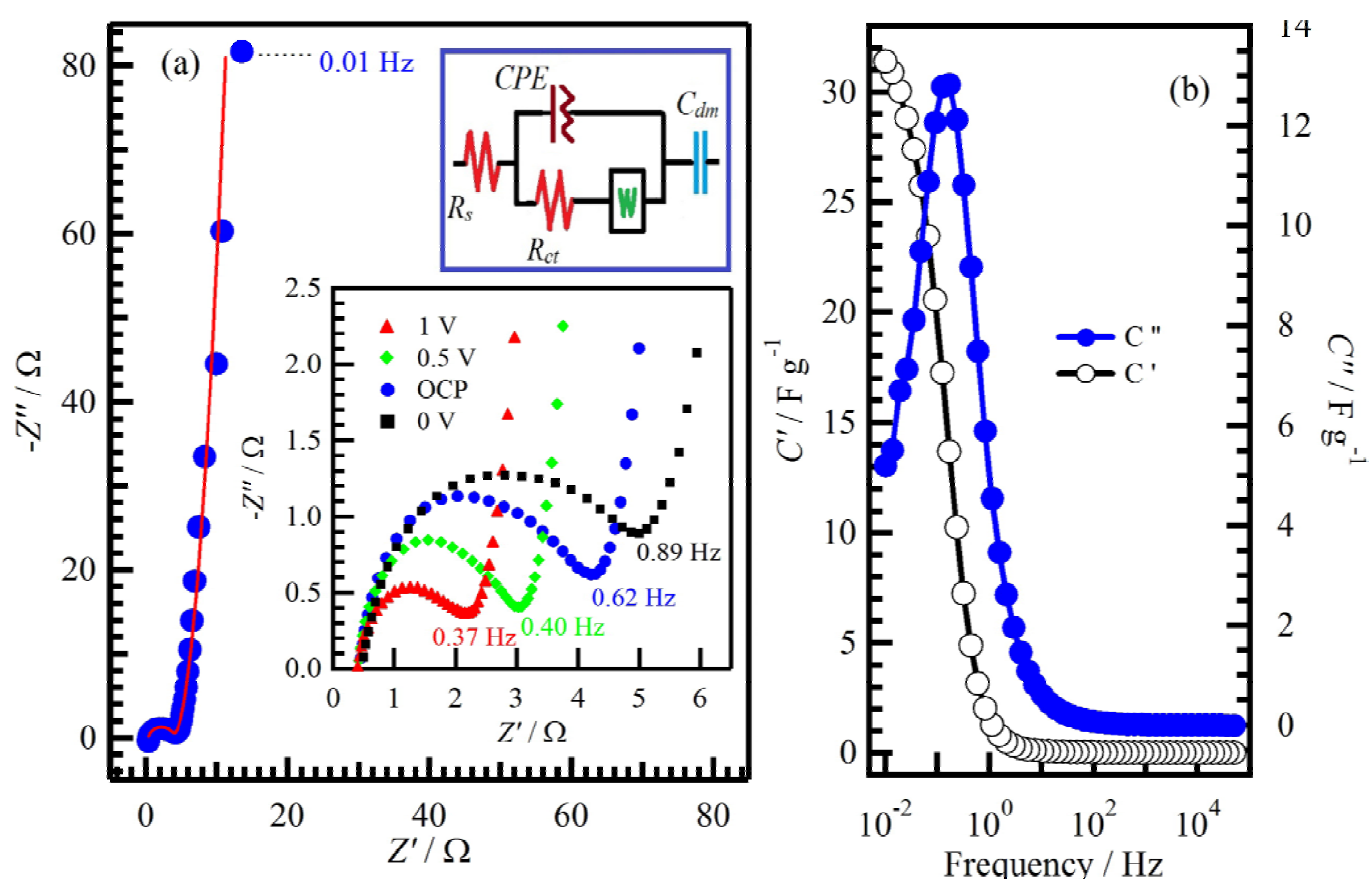


Fig. 11. *Nyquist* plot (a) of GNS at OCP, the insets are the high-frequency region of the plot at different operating voltages and the equivalent circuit and (b) real and imaginary parts of the capacitance as functions of the frequency, the solid line is the fitting data.

Table 1. Fit parameters of the experimental complex impedance data.

Potential	$R_s(\Omega)$	$R_{ct}(\Omega)$	CPE(mF)	$C_{dm}(mF)$	$W(\Omega)$	$S_E(m^2 g^{-1})$	$\tau(s)$
0	0.44	4.14	0.82	186	0.28	128.8	8.1
OCP	0.38	3.60	0.72	216	0.38	161.3	5.9
0.5	0.39	2.51	0.61	236	0.50	174.9	5.9
1	0.39	1.73	1.66	255	0.46	199.1	4.3

circuit potential (OCP) of 4 mV. The insets are the equivalent circuit and the zoomed view of the high-frequency region for data measured at OCP and other applied potentials. The *Nyquist* plot shows a semi-circle in the high frequency region and a vertical line (84°) at low frequency, in accordance with Warburg diffusion related to the diffusion of electrolyte within the pores of the electrode. The near-vertical slope at the low frequency region indicates good capacitor behaviour of the cell. The equivalent circuit is composed of a solution resistor (R_s), an electrode-electrolyte interfacial charge transfer resistor (R_{ct}), a constant phase element (CPE), a Warburg diffusion element (W), and a faradic capacitor (C_{dm}). R_s value was obtained from the fitting as the intercept on the real axis of the high frequency range and R_{ct} was estimated from the diameter of the semi-circle. R_s , R_{ct} , and other fitting parameters are summarized in Table 1. R_s and R_{ct} for GNS at OCP were found to be 0.39 and 3.61 Ω , respectively. The R_s was almost the same for different applied potentials, whereas R_{ct} decreases with increasing the potential.

The electrochemical active specific surface area (S_E) can be calculated as $S_E = C_d / C_{dl}$, where, C_d is a constant value of 20 $\mu F cm^{-2}$ [34], C_{dl} was obtained from impedance data in low frequency (0.01 Hz) according to the equation $C_{dl} = 1 / (2\pi f m Z'')$, f is the frequency, Z'' is the imaginary part in the impedance, and m is the mass of the active material. The calculated value of S_E at OCP was found to be 161.3 $m^2 g^{-1}$, which is 30% higher than that obtained from BET (124.1 $m^2 g^{-1}$). Moreover, S_E was found to increase with increasing applied voltage.

The complex model of the capacitance was studied to show the dependence of the specific capacitance on frequency. The cell capacitance can be expressed as real (C') and imaginary (C'') parts according to the following equations [6,30-32]: $C'(\omega) = -Z''(\omega) / \omega |Z(\omega)|^2$ and $C''(\omega) = Z'(\omega) / \omega |Z(\omega)|^2$, where, $\omega = 2\pi f$. Plots of C' and C'' as functions of frequency are shown in Fig.11b. The relaxation time ($\tau = 1/f_0$) was calculated from the frequency (f_0) corresponding to the maximum energy dissipation in Fig. 11.

The τ values were found to be 5.9 s, indicating good electrochemical supercapacitance properties, and fast charge–discharge characteristic response. The τ value distinguishes the transition between resistive and capacitive behaviors, as it defines predominantly resistive behavior at frequencies above $1/\tau$ and capacitive behavior below $1/\tau$. The τ of the present sample is lower than 8 s found for activated carbon-based electrodes and is very close to 4.9 s obtained for carbon nanotubes [6,30-32].

4. CONCLUSION

Various techniques have been used to characterize the structure and morphology of the graphene nanosheets synthesized by the reduction of a graphite oxide. The mesoporous structure of the nanosheets was confirmed by FESEM and N_2 adsorption-desorption measurements. The specific capacitance of graphene nanosheets was 140 F g^{-1} at 0.05 A g^{-1} . Graphene nanosheets show a high cyclic stability of about 86% over 1100 cycles at 1 A g^{-1} . Lower solution resistance and charge transfer resistance were obtained by analysing the impedance spectra, indicating good electrochemical properties of these graphene nanosheets. The electrochemical active specific surface area was found to be 161.3 $m^2 g^{-1}$ which is 30% higher than that obtained from BET measurements. Finally, such characteristics support the suitability of the present material for supercapacitor electrode applications.

ACKNOWLEDGEMENTS

K.F. Chong and co-workers would like to acknowledge the funding from the Ministry of Education Malaysia in the form of MTUN-COE grants (RDU121212 & RDU121213) and RACE grant (RDU141309).

REFERENCES

- [1] Y. Zhang, H. Feng, X. Wu, L. Wang, A. Zhang, T. Xia, H. Dong, X. Li and L. Zhang // *Int. J. Hydrogen Energy* **34** (2009) 4889.

- [2] Z. Song, W. Liu, M. Zhao, Y. Zhang, G. Liu, C. Yu and J. Qiu // *J. Alloys Compd.* **560** (2013) 151.
- [3] G.A.M. Ali, O.A. Fouad, S.A. Makhlouf, M.M. Yusoff and K.F. Chong // *J. Solid State Electrochem.* **18** (2014) 2505.
- [4] J. Yan, T. Wei, B. Shao, F. Ma, Z. Fan, M. Zhang, C. Zheng, Y. Shang, W. Qian and F. Wei // *Carbon* **48** (2010) 1731.
- [5] G.A.M. Ali, S.A.B.A. Manaf, A. Kumar, K.F. Chong and G. Hegde // *J. Phys. D: Appl. Phys.* **47** (2014) 495307.
- [6] C. Portet, P.L. Taberna, P. Simon, E. Flahaut and C. Laberty-Robert // *Electrochim. Acta* **50** (2005) 4174.
- [7] G.A.M. Ali, L.L. Tan, R. Jose, M.M. Yusoff and K.F. Chong // *Mater. Res. Bull.* **60** (2014) 5.
- [8] A. Ponrouch, S. Garbarino, E. Bertin and D. Guay // *J. Power Sources* **221** (2013) 228.
- [9] Q.T. Qu, Y. Shi, L.L. Li, W.L. Guo, Y.P. Wu, H.P. Zhang, S.Y. Guan and R. Holze // *Electrochem. Commun.* **11** (2009) 1325.
- [10] I. Jureviciute and S. Bruckenstein // *J. Solid State Electrochem.* **7** (2003) 554.
- [11] D.S. Patil, S.A. Pawar, R.S. Devan, M.G. Gang, Y.-R. Ma, J.H. Kim and P.S. Patil // *Electrochim. Acta* **105** (2013) 569.
- [12] M.D. Stoller, S. Park, Y. Zhu, J. An and R.S. Ruoff // *Nano Letter* **8** (2008) 3498.
- [13] C. Liu, Z. Yu, D. Neff, A. Zhamu and B.Z. Jang // *Nano Letter* **10** (2010) 4863.
- [14] O.C. Compton and S.T. Nguyen // *Small* **6** (2010) 711.
- [15] S. Park, J. An, J.R. Potts, A. Velamakanni, S. Murali and R.S. Ruoff // *Carbon* **49** (2011) 3019.
- [16] J. Yang and S. Gunasekaran // *Carbon* **51** (2013) 36.
- [17] B. Zhao, P. Liu, Y. Jiang, D. Pan, H. Tao, J. Song, T. Fang and W. Xu // *J. Power Sources* **198** (2012) 423.
- [18] H.N. Tien, V.H. Luan, T.K. Lee, B.-S. Kong, J.S. Chung, E.J. Kim and S.H. Hur // *Chemical Engineering Journal* **211-212** (2012) 97.
- [19] F.Y. Ban, S.R. Majid, N.M. Huang and H.N. Lim // *Int. J. Electrochem. Sci.* **7** (2012) 4345.
- [20] S.-H. Lee, S.-D. Seo, K.-S. Park, H.-W. Shim and D.-W. Kim // *Mater. Chem. Phys.* **135** (2012) 309.
- [21] L. Chen, Z. Xu, J. Li, C. Min, L. Liu, X. Song, G. Chen and X. Meng // *Mater. Lett.* **65** (2011) 1229.
- [22] L. Tang, Y. Wang, Y. Li, H. Feng, J. Lu and J. Li // *Adv. Funct. Mater.* **19** (2009) 2782.
- [23] X. Wang and W. Dou // *Thermochim. Acta* **529** (2012) 25.
- [24] N.A. Kumar, H.J. Choi, Y.R. Shin, D.W. Chang, L. Dai and J.B. Baek // *ACS Nano* **6** (2012) 1715.
- [25] J. Shen, M. Shi, H. Ma, B. Yan, N. Li, Y. Hu and M. Ye // *J. Colloid Interface Sci.* **352** (2010) 366.
- [26] D. Zhang, X. Zhang, Y. Chen, C. Wang and Y. Ma // *Electrochim. Acta* **69** (2012) 364.
- [27] T. Liu, Y. Li, Q. Du, J. Sun, Y. Jiao, G. Yang, Z. Wang, Y. Xia, W. Zhang, K. Wang, H. Zhu and D. Wu // *Colloids Surf B Biointerfaces* **90** (2012) 197.
- [28] S.H. Aboutalebi, M. Salari, K. Konstantinov, D. Wexler, H.K. Liu and S.X. Dou // *Energy & Environmental Science* **4** (2011) 1855.
- [29] G. Wang, B. Wang, J. Park, J. Yang, X. Shen and J. Yao // *Carbon* **47** (2009) 68.
- [30] Z. Bo, Z. Wen, H. Kim, G. Lu, K. Yu and J. Chen // *Carbon* **50** (2012) 4379.
- [31] M.D. Stoller and R.S. Ruoff // *Energy & Environmental Science* **3** (2010) 1294.
- [32] J. Zhang, T. Tian, Y. Chen, Y. Niu, J. Tang and L.-C. Qin // *Chem. Phys. Lett.* **591** (2014) 78.
- [33] M.S. Kishore, P. Srimathi, S. Kumar, S. Addepalli, S. Swaminathan, V. Tilak and R. Colborn // *Bull. Mater. Sci.* **36** (2013) 667.
- [34] S. Chou, F. Cheng and J. Chen // *J. Power Sources* **162** (2006) 727.